Plasmon-induced transparency in metal–insulator–metal waveguide side-coupled with multiple cavities

Jing Guo

State Key Laboratory of Transient Optics and Photonics, Xi'an Institute of Optics and Precision Mechanics, Chinese Academy of Sciences, Xi'an 710119, China (guojing@opt.ac.cn)

Received 17 October 2013; revised 5 January 2014; accepted 15 January 2014; posted 4 February 2014 (Doc. ID 199716); published 6 March 2014

We have demonstrated the analogue of electromagnetically induced transparency (EIT) in the metal–insulator–metal plasmonic waveguide, which consists of a bus waveguide side-coupled with a series of slot cavities. By finite-difference time-domain simulations, it is found that the resonance wavelength of the slot cavity can be controlled by adjusting the length of the cavity. Moreover, the EIT-like response is strongly dependent on the coupling separation between the corresponding adjacent cavities. Multiple-peak plasmon-induced transparency can be realized by cascading multiple cavities with different lengths and suitable cavity–cavity separations. This ultracompact plasmonic waveguide system may find important applications for multichannel plasmonic filter, nanoscale optical switching, and slow-light devices in highly integrated optical circuits and networks. © 2014 Optical Society of America

OCIS codes: (240.6680) Surface plasmons; (230.4555) Coupled resonators; (260.5740) Resonance.
http://dx.doi.org/10.1364/AO.53.001604

1. Introduction

Electromagnetic waves trapped on metal–dielectric interfaces and coupled to propagating free electron oscillations on the surface of metals are known as surface plasmon polaritons (SPPs), which are regarded as having the most potential for realization of highly integrated optical circuits due to the manipulation of light in a nanoscale domain and overcoming of the classical diffraction limit [1,2]. A large amount of devices based on SPPs, such as Mach–Zehnder interferometers [2,3], all-optical switches [4–7], splitters [2,8,9], modulators [10,11], sensors [12,13], beam manipulators [14,15], metallic superlens [16], filters [17–21], polarization analyzers [22], optical amplifiers [23], optical buffers [24,25], Bragg reflectors [26–30], mirrors [31], and demultiplexers [32–37], have been demonstrated experimentally and simulated numerically. Metal–insulator–metal (MIM) waveguides have strong light confinement with an acceptable length for SPP propagation [38–42]. They are promising structures for design of nanoscale all-optical devices due to their relatively easy fabrication according to the current state of the art [43]. Optical resonators are crucial structural components in plasmonic wavelength-selective devices owing to their symmetry, simplicity, and ease of fabrication [44]. Electromagnetically induced transparency (EIT) occurs in the atomic system due to the quantum interference between the different excitation pathways to atomic levels [45,46]. Theoretical analysis and experimental observations demonstrate that a novel phenomenon analogous to EIT can also occur in the optical resonator systems owing to the coherent interference of coupled resonators [47–49]. The footprint and field confinement of these photonic EIT devices are limited by the classical diffraction limit [39]. Recently, EIT-like effects have been found in the plasmonic structures [50–52]. In particular, the plasmonic analogous to EIT has also been investigated in the MIM waveguide-resonator systems [53–56]. For

1559-128X/14/081604-06$15.00/0

example, Lu *et al.* reported a significant optical effect analogous to EIT in the nanoscale plasmonic resonator system consisting of a slot cavity as well as bus and resonant waveguides [53]. Wang *et al.* found that the incident pulse can be slowed down without distortion in the MIM plasmonic waveguide based on a plasmonic analogue of EIT [55]. The plasmonic EIT-like response also enables the realization of nanoscale band-pass filters with multiple channels in MIM waveguides [56].

In the paper, we have numerically investigated the analogue of EIT in the MIM plasmonic waveguide, which consists of a bus MIM waveguide perpendicularly side-coupled with a series of slot cavities. The resonance wavelength of each cavity can be tuned by changing the length of the cavity. It is found that the EIT-like response is dependent on the coupling separation between the corresponding adjacent cavities. Multiple-peak plasmon-induced transparency can be realized by cascading multiple cavities with different lengths and special separations. The results can pave the way for the design of multiple-channel plasmonic filters.

2. Structure Model and Theory

As shown in Fig. 1, the MIM waveguide consists of two metallic claddings, a dielectric core with width w, and multiple rectangular cavities. The insulator in the dielectric core and cavities is set as air. The metal is assumed as silver, whose relative permittivity can be described by the well-known Drude model [29,57],

$$\varepsilon_m(\omega) = \varepsilon_\infty - \frac{\omega_p^2}{\omega(\omega + i\gamma)}, \tag{1}$$

where ε_∞ represents the dielectric constant at the infinite frequency, and ω_p and γ are the bulk plasma and electron collision frequencies, respectively. ω is the angular frequency of incident light. The parameters for silver can be set as $\varepsilon_\infty = 3.7$, $\omega_p = 9.1$ eV, and $\gamma = 0.018$ eV[26]. There exist two types of SPP modes in MIM waveguides. One is the symmetric mode, and the other is the antisymmetric mode. Here, the terminology is based on the longitudinal electric field (E_x). Hence, both the transverse electric (TE) field (E_y) and the transverse magnetic (TM) field (H_z) exhibit antisymmetric distributions at the symmetric mode and symmetric distributions at the antisymmetric mode [26]. The symmetric mode performs a cutoff when w decreases below a width of about hundreds of nanometers [26]. As the width of the waveguide in our structure is below the cutoff width, only the antisymmetric mode is considered here. When a TM-polarized plane wave is impinged to the MIM structure, the incident wave is coupled into the waveguide and the SPP wave forms on the metal interfaces. The incident power is partly coupled into the nanocavity nearby the bus waveguide. The nanocavity as a function of the resonator can stop the light signal with the resonance wavelength. The transmission spectrum of the waveguide will exhibit a dip (i.e., transmitted dip) at the resonance wavelength. Here, the transmission characteristics of the MIM waveguide are investigated by the finite-difference time-domain (FDTD) method with perfectly matched layer (PML) absorbing boundary conditions [58]. The dispersive property of silver is described by the above Drude model in FDTD simulations. In the FDTD method, the spatial steps are set as $\Delta x = 2$ nm and $\Delta y = 2$ nm. The temporal step is $\Delta t = \Delta x/2c$ [6]. The gap width g and slit width w are set as 10 and 50 nm, respectively. P_{in} presents the incident power at the position P. P_{out} is output power at the position Q. The transmission is defined as $T = P_{\text{out}}/P_{\text{in}}$. The dispersion relation of the SPP mode in the MIM waveguide can be expressed as follows [26,57]:

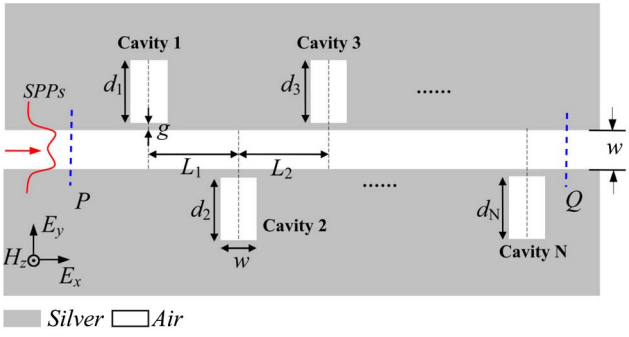

Fig. 1. Schematic diagram of plasmonic waveguide system. w and g are the widths of the metallic slit and gap, respectively. d_i is the length of cavity $i (i = 1, 2, \ldots, N)$. L_i represents the separation between cavities i and $i + 1$.

$$\varepsilon_m k_d \tanh\left(\frac{wk_d}{2}\right) + \varepsilon_d k_m = 0, \tag{2}$$

$$k_{d,m} = \sqrt{\beta_{\text{spp}}^2 - \varepsilon_{d,m} k_0^2}, \tag{3}$$

$$n_{\text{eff}} = \beta_{\text{spp}}/k_0, \tag{4}$$

where k_m and k_d are transverse propagation constants of the metal and dielectric. ε_m and ε_d are the dielectric constants of metal and cavity, respectively. β_{spp} stands for the complex propagation constant of the SPP wave, which is obtained by substituting Eq. (3) into Eq. (2). The detailed value can be calculated through numerical solution. $k_0 = 2\pi/\lambda$ is the wave vector of incident light. n_{eff} denotes the effective refractive index of the SPP mode, which is described in Fig. 2(a).

3. Results and Analysis

We use the FDTD method to investigate the transmission properties of the MIM plasmonic waveguide side-coupled with cavities. As shown in Fig. 3(a), the MIM waveguide side-coupled with one cavity can act as an optical band-stop filter. By changing the

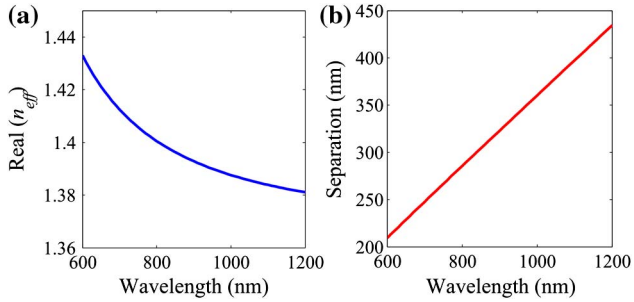

Fig. 2. (a) Real part of the effective refractive index of SPP wave with $w = 50$ nm. (b) Separations between adjacent cavities at different central wavelengths with most obvious EIT-like response.

geometrical parameter d, which represents the length of the cavity, the operating (resonant) wavelength can be effectively manipulated. As can be seen in Fig. 3(b), the operating wavelength has a linear relationship with the cavity length.

For a dual-cavity-coupled waveguide system, the transmission spectra with different cavity–cavity separations L are calculated and shown in Fig. 4(a). Here, the lengths of two cavities are fixed as $d_1 = 150$ nm and $d_2 = 170$ nm. The incident lights at the resonant wavelengths of the cavities will be reflected; thus the spectrum possesses two transmitted dips, as shown in Fig. 4(a). One can also clearly see that there is a transmission peak between the transmitted dips, which is relative with the separation L. When a Fabry–Perot (F-P) resonance builds in the bus waveguide between two cavities, the transmission exhibits the most obvious EIT-like response. The optimized separation between the two cavities can be expressed as

$$L = \frac{\lambda}{2\,\mathrm{Re}(n_{\mathrm{eff}}(\lambda))}. \tag{5}$$

Figure 2(b) depicts the optimized separations at different central wavelengths with obvious EIT-like response. As shown in Fig. 4(a), when the separation of the cavities is an optimized value $L = 215$ nm, a high and narrow transmission peak displays in the transmission spectrum. The cavity quality factor is expressed as $Q = \lambda_0/\Delta\lambda$, which is a very important parameter for the filtering peak. Here, λ_0 and $\Delta\lambda$ stand for the peak wavelength and the full width at half maximum of the transmission spectrum, respectively. As depicted in Fig. 4(a), the Q factor is equal to ~25 with $L = 215$ nm. However, the transmission peak is prohibited when $L = 105$ and 150 nm, where the F-P resonance cannot be established. The field distribution of $|H_z|$ for the transparency-resonance wavelength is shown in Fig. 4(b), which clearly depicts the resonance between two cavities, and the SPP wave can pass through the plasmonic waveguide.

Adding another cavity with $d_3 = 190$ nm on the right side of the dual-cavity-coupled waveguide structure, a three-cavity-coupled system is formed, when the cavity–cavity separations are set as the

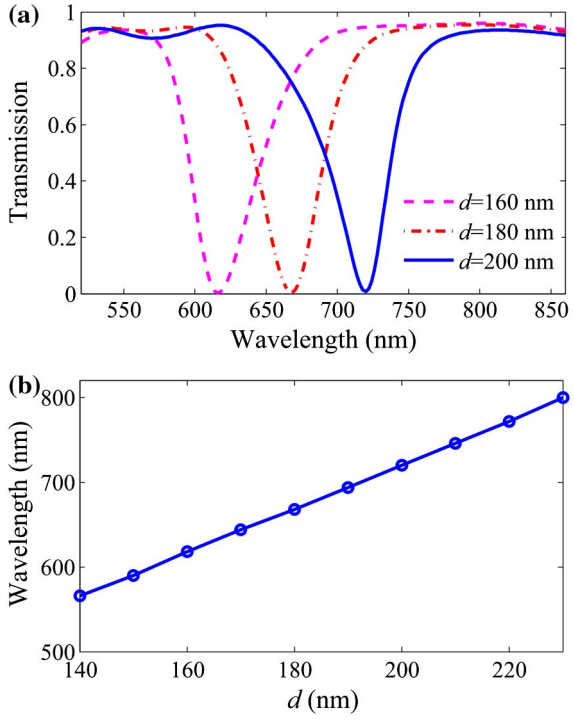

Fig. 3. (a) Transmission spectrum of MIM waveguide structure for different cavity lengths d with $g = 10$ nm and $w = 50$ nm. (b) Operating wavelength versus the cavity length d.

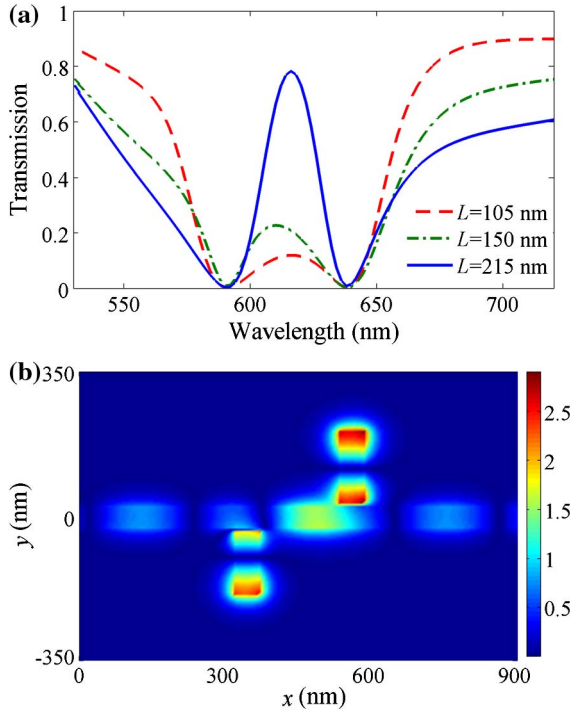

Fig. 4. (a) Transmission spectrum with different cavity–cavity separations in dual-cavity-coupled waveguide system with $d_1 = 150$ nm, $d_2 = 170$ nm, $g = 10$ nm, and $w = 50$ nm. (b) Field distribution of $|H_z|$ at transparency-peak wavelength in dual-cavity-coupled waveguide with $L = 215$ nm.

optimized values $L_1 = 215$ nm and $L_2 = 235$ nm. Dual induced-transparency peaks appear in the transmission spectrum, as shown in Fig. 5(a). The appearance of the first EIT-like peak at the wavelength of $\lambda_1 = 617$ nm is a result of the F-P resonance building in the bus waveguide between two left cavities. Another EIT-like peak at the wavelength of $\lambda_2 = 670$ nm emerges because of the satisfaction of the F-P resonant condition in the bus waveguide between two right cavities. These results can be verified by the field distributions at the wavelengths of transparency peaks, as shown in Figs. 5(b) and 5(c). The EIT-like transmission peaks possess a slight decrease when the number of coupled cavities increases, as can be seen in Figs. 4(a) and 5(a). When the incident wavelength locates at the transparency peaks, the SPP waves can pass through the plasmonic waveguide system, which is in accordance with Fig. 5(a).

The above principle yet applies to multi-cavity-coupled plasmonic waveguides. Thus, a plasmonic four-cavity-coupled waveguide system is designed as an example to display the multipeak EIT-like spectral response. The lengths of cavities 1, 2, 3, and 4 are fixed as $d_1 = 150$ nm, $d_2 = 170$ nm, $d_3 = 190$ nm, and $d_4 = 215$ nm, respectively. The

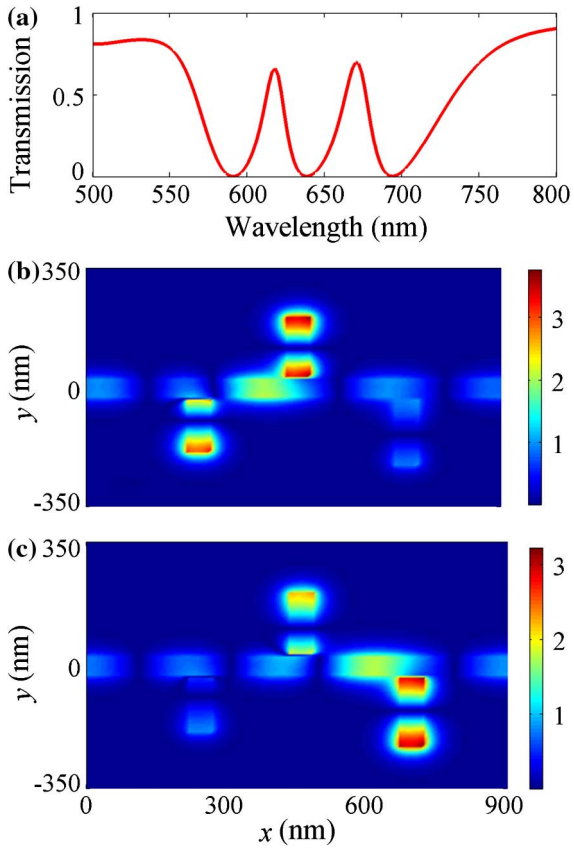

Fig. 5. (a) Transmission spectrum in the triple-cavity-coupled waveguide system with $d_1 = 150$ nm, $d_2 = 170$ nm, $d_3 = 190$ nm, $L_1 = 215$ nm, $L_2 = 235$ nm, $g = 10$ nm, and $w = 50$ nm. (b), (c) Field distributions of $|H_z|$ with incident wavelengths of 617 and 670 nm.

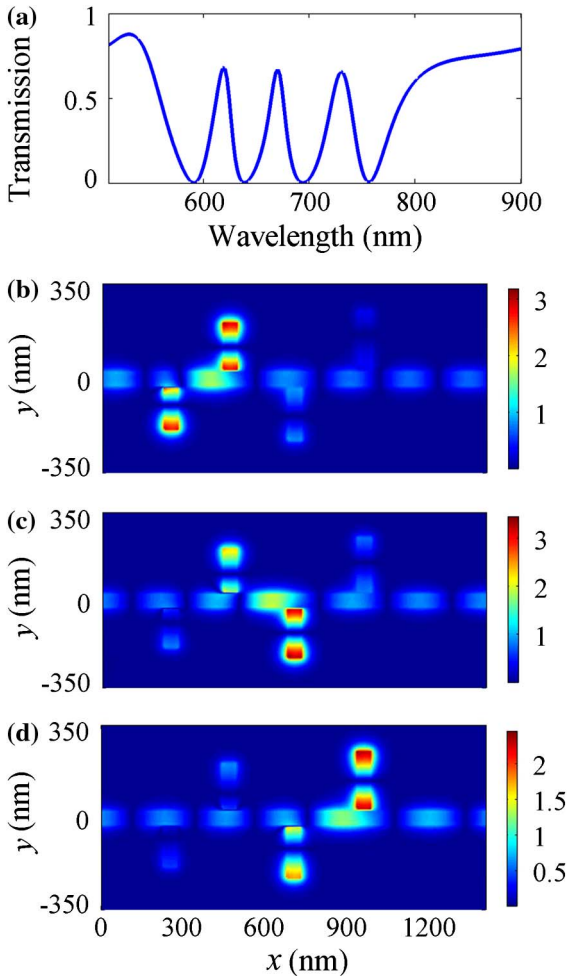

Fig. 6. (a) Transmission spectrum for the four-cavity-coupled waveguide system with $d_1 = 150$ nm, $d_2 = 170$ nm, $d_3 = 190$ nm, $d_4 = 215$ nm, $L_1 = 215$ nm, $L_2 = 235$ nm, $L_3 = 255$ nm, $g = 10$ nm, and $w = 50$ nm. (b)–(d) Field distributions of $|H_z|$ with incident wavelengths of 617, 670, and 730 nm.

separations of adjacent cavities L_1, L_2, and L_3 are 215, 235, and 255 nm, respectively. g and w are 10 and 50 nm, respectively. By the FDTD simulations, there are three EIT-like transmission peaks at the wavelengths of 617, 670, and 730 nm in the transmission spectrum, as shown in Fig. 6(a). The EIT-like peak appears when the corresponding F-P resonant condition is satisfied in the MIM waveguide between adjacent cavities, which is verified by the field distributions at the transparency-peak wavelengths in Figs. 6(b)–6(d). The above samples are only examples of multi-cavity-coupled waveguide systems. $N-1$ areas of EIT-like transparency windows can be realized in the MIM plasmonic waveguide with N side-coupled cavities. The EIT-like effects in the metallic nanostructures were employed to enhance the nonlinear effects [59,60] and plasmonic sensing [61]. The multi-peak EIT-like response contributes to the realization of a high-channel-count band-pass filter. It is found that our design is simpler than that reported in Ref. [56].

4. Conclusion

In summary, we have proposed and numerically investigated a plasmonic waveguide system to generate EIT-like response in a MIM plasmonic waveguide system consisting of a bus waveguide side-coupled with a series of slot cavities. Our simulation results reveal that the resonance wavelength of the slot cavity can be controlled by tuning the cavity length. Obvious plasmon-induced transparency will emerge when the plasmonic waveguide between adjacent cavities satisfies the resonant condition. Multiple-peak induced transparency can be realized by cascading multiple cavities with different lengths and separations. The proposed plasmonic waveguide system will find potential applications in highly integrated optical devices, such as nanoscale multi-channel plasmonic filter, optical switching, and slow-light components.

This work was supported by the National Natural Science Foundation of China under grants 61223007 and 11204368.

References

1. W. L. Barnes, A. Dereux, and T. W. Ebbesen, "Surface plasmon subwavelength optics," Nature **424**, 824–830 (2003).
2. S. I. Bozhevolnyi, V. S. Volkov, E. Devaux, J. Y. Laluet, and T. W. Ebbesen, "Channel plasmon subwavelength waveguide components including interferometers and ring resonators," Nature **440**, 508–511 (2006).
3. B. Wang and G. P. Wang, "Surface plasmon polariton propagation in nanoscale metal gap waveguides," Opt. Lett. **29**, 1992–1994 (2004).
4. H. Lu, X. Liu, L. Wang, Y. Gong, and D. Mao, "Ultrafast all-optical switching in nanoplasmonic waveguide with Kerr nonlinear resonator," Opt. Express **19**, 2910–2915 (2011).
5. G. A. Wurtz, R. Pollard, and A. V. Zayats, "Optical bistability in nonlinear surface-plasmon polaritonic crystals," Phys. Rev. Lett. **97**, 057402 (2006).
6. H. Lu, X. M. Liu, Y. K. Gong, D. Mao, and L. R. Wang, "Optical bistability in metal–insulator–metal plasmonic Bragg waveguides with Kerr nonlinear defects," Appl. Opt. **50**, 1307–1311 (2011).
7. G. Wang, H. Lu, X. Liu, and Y. Gong, "Numerical investigation of an all-optical switch in a graded nonlinear plasmonic grating," Nanotechnology **23**, 444009 (2012).
8. G. Veronis and S. Fan, "Bends and splitters in metal-dielectric-metal subwavelength plasmonic waveguides," Appl. Phys. Lett. **87**, 131102 (2005).
9. G. Veronis, Z. Yu, S. E. Kocabas, D. A. B. Miller, M. L. Brongersma, and S. Fan, "Metal-dielectric-metal plasmonic waveguide devices for manipulating light at the nanoscale," Chin. Opt. Lett. **7**, 302–308 (2009).
10. T. Nikolajsen, K. Leosson, and S. I. Bozhevolnyi, "Surface plasmon polariton based modulators and switches operating at telecom wavelengths," Appl. Phys. Lett. **85**, 5833–5835 (2004).
11. X. Piao, S. Yu, and N. Park, "Control of Fano asymmetry in plasmon induced transparency and its application to plasmonic waveguide modulator," Opt. Express **20**, 18994–18999 (2012).
12. K. Donghyun, "Effect of the azimuthal orientation on the performance of grating-coupled surface-plasmon resonance biosensors," Appl. Opt. **44**, 3218–3223 (2005).
13. H. Lu, X. M. Liu, D. Mao, and G. X. Wang, "Plasmonic nanosensor based on Fano resonance in waveguide-coupled resonators," Opt. Lett. **37**, 3780–3782 (2012).
14. H. Kim, J. Park, and B. Lee, "Tunable directional beaming from subwavelength metal slits with metal–dielectric composite surface gratings," Opt. Lett. **34**, 2569–2571 (2009).
15. L. L. Yin, V. K. Vlasko-Vlasov, J. Pearson, J. M. Hiller, J. Hua, U. Welp, D. E. Brown, and C. W. Kimball, "Subwavelength focusing and guiding of surface plasmons," Nano Lett. **5**, 1399–1402 (2005).
16. G. Tremblay and Y. Sheng, "Improving imaging performance of a metallic superlens using the long-range surface plasmon polariton mode cutoff technique," Appl. Opt. **49**, A36–A41 (2010).
17. H. Lu, X. M. Liu, D. Mao, L. R. Wang, and Y. K. Gong, "Tunable band-pass plasmonic waveguide filters with nanodisk resonators," Opt. Express **18**, 17922–17927 (2010).
18. A. Hosseini and Y. Massoud, "Nanoscale surface plasmon based resonator using rectangular geometry," Appl. Phys. Lett. **90**, 181102 (2007).
19. S. S. Xiao, L. Liu, and M. Qiu, "Resonator channel drop filters in a plasmon-polaritons metal," Opt. Express **14**, 2932–2937 (2006).
20. H. Lu, X. Liu, Y. Gong, L. Wang, and D. Mao, "Multi-channel plasmonic waveguide filters with disk-shaped nanocavities," Opt. Commun. **284**, 2613–2616 (2011).
21. Z. Han, V. Van, W. N. Herman, and P. T. Ho, "Aperture-coupled MIM plasmonic ring resonators with sub-diffraction modal volumes," Opt. Express **17**, 12678–12684 (2009).
22. S. Y. Yang, W. Chen, R. L. Nelson, and Q. Zhan, "Miniature circular polarization analyzer with spiral plasmonic lens," Opt. Lett. **34**, 3047–3049 (2009).
23. I. D. Leon and P. Berini, "Amplification of long-range surface plasmons by a dipolar gain medium," Nat. Photonics **10**, 1–6 (2010).
24. Q. Q. Gan, Y. J. Ding, and F. J. Bartoli, "'Rainbow' trapping and releasing at telecommunication wavelengths," Phys. Rev. Lett. **102**, 056801 (2009).
25. G. Wang, H. Lu, and X. Liu, "Trapping of surface plasmon waves in graded grating waveguide system," Appl. Phys. Lett. **101**, 013111 (2012).
26. J. Park, H. Kim, and B. Lee, "High order plasmonic Bragg reflection in the metal-insulator-metal waveguide Bragg grating," Opt. Express **16**, 413–425 (2008).
27. Y. K. Gong, L. R. Wang, X. H. Hu, X. H. Li, and X. M. Liu, "Broad-bandgap and low-sidelobe surface plasmon polariton reflector with Bragg-grating-based MIM waveguide," Opt. Express **17**, 13727–13736 (2009).
28. Y. K. Gong, X. Liu, and L. Wang, "High-channel-count plasmonic filter with the metal-insulator-metal Fibonacci-sequence gratings," Opt. Lett. **35**, 285–287 (2010).
29. Z. Han, E. Forsberg, and S. L. He, "Surface plasmon Bragg gratings formed in metal-insulator-metal waveguides," IEEE Photon. Technol. Lett. **19**, 91–93 (2007).
30. J. Park, H. Kim, I. M. Lee, S. Kim, J. Jung, and B. Lee, "Resonant tunneling of surface plasmon polariton in the plasmonic nano-cavity," Opt. Express **16**, 16903–16915 (2008).
31. S. Randhawa, M. U. González, J. Renger, S. Enoch, and R. Quidant, "Design and properties of dielectric surface plasmon Bragg mirrors," Opt. Express **18**, 14496–14510 (2010).
32. H. Lu, X. Liu, Y. Gong, D. Mao, and L. Wang, "Enhancement of transmission efficiency of nanoplasmonic wavelength demultiplexer based on channel drop filters and reflection nanocavities," Opt. Express **19**, 12885–12890 (2011).
33. J. Tao, X. G. Huang, and J. H. Zhu, "A wavelength demultiplexing structure based on metal-dielectric-metal plasmonic nano-capillary resonators," Opt. Express **18**, 11111–11116 (2010).
34. G. Wang, H. Lu, X. M. Liu, D. Mao, and L. N. Duan, "Tunable multi-channel wavelength demultiplexer based on MIM plasmonic nanodisk resonators at telecommunication regime," Opt. Express **19**, 3513–3518 (2011).
35. A. Drezet, D. Koller, A. Hohenau, A. Leitner, F. R. Aussenegg, and J. R. Krenn, "Plasmonic crystal demultiplexer and multiports," Nano Lett. **7**, 1697–1700 (2007).
36. A. Noual, A. Akjouj, Y. Pennec, J. N. Gillet, and B. Djafari-Rouhani, "Modeling of two-dimensional nanoscale Y-bent plasmonic waveguides with cavities for demultiplexing of the telecommunication wavelengths," New J. Phys. **11**, 103020 (2009).

37. H. Lu, X. Liu, D. Mao, Y. Gong, and G. Wang, "Analysis of nanoplasmonic wavelength demultiplexing based on metal–insulator–metal waveguides," J. Opt. Soc. Am. B **28**, 1616–1621 (2011).
38. P. Neutens, P. V. Dorpe, I. D. Vlaminck, L. Lagae, and G. Borghs, "Electrical detection of confined gap plasmons in metal-insulator-metal waveguides," Nat. Photonics **3**, 283–286 (2009).
39. R. Zia, J. A. Schuller, A. Chandran, and M. L. Brongersma, "Plasmonics: the next chip-scale technology," Mater. Today **9**(7–8), 20–27 (2006).
40. A. Chandran, E. S. Barnard, J. S. White, and M. L. Brongersma, "Metal-dielectric-metal surface plasmon-polariton resonators," Phys. Rev. B **85**, 085416 (2012).
41. J. Park, K. Y. Kim, I. M. Lee, H. Na, S. Y. Lee, and B. Lee, "Trapping light in plasmonic waveguides," Opt. Express **18**, 598–623 (2010).
42. G. Wang, H. Lu, and X. Liu, "Gain-assisted trapping of light in tapered plasmonic waveguide," Opt. Lett. **38**, 558–560 (2013).
43. J. A. Dionne, L. A. Sweatlock, H. A. Atwater, and A. Polman, "Plasmon slot waveguides: towards chip-scale propagation with subwavelength scale localization," Phys. Rev. B **73**, 035407 (2006).
44. I. Chremmos, "Magnetic field integral equation analysis of interaction between a surface plasmon polariton and a circular dielectric cavity embedded in the metal," J. Opt. Soc. Am. A **26**, 2623–2633 (2009).
45. K. J. Boller, A. Imamolu, and S. E. Harris, "Observation of electromagnetically induced transparency," Phys. Rev. Lett. **66**, 2593–2596 (1991).
46. M. Fleischhauer, A. Imamoglu, and J. P. Marangos, "Electromagnetically induced transparency: optics in coherent media," Rev. Mod. Phys. **77**, 633–673 (2005).
47. Q. Xu, S. Sandhu, M. L. Povinelli, J. Shakya, S. Fan, and M. Lipson, "Experimental realization of an on-chip all-optical analogue to electromagnetically induced transparency," Phys. Rev. Lett. **96**, 123901 (2006).
48. K. Totsuka, N. Kobayashi, and M. Tomita, "Slow light in coupled-resonator-induced transparency," Phys. Rev. Lett. **98**, 213904 (2007).
49. X. Yang, M. Yu, D. L. Kwong, and C. W. Wong, "All-optical analog to electromagnetically induced transparency in multiple coupled photonic crystal cavities," Phys. Rev. Lett. **102**, 173902 (2009).
50. R. D. Kekatpure, E. S. Barnard, W. Cai, and M. L. Brongersma, "Phase-coupled plasmon induced transparency," Phys. Rev. Lett. **104**, 243902 (2010).
51. S. Zhang, D. A. Genov, Y. Wang, M. Liu, and X. Zhang, "Plasmon-induced transparency in metamaterials," Phys. Rev. Lett. **101**, 047401 (2008).
52. N. Liu, L. Langguth, T. Weiss, J. Kästel, M. Fleischhauer, T. Pfau, and H. Giessen, "Plasmonic analogue of electromagnetically induced transparency at the Drude damping limit," Nat. Mater. **8**, 758–762 (2009).
53. H. Lu, X. Liu, D. Mao, Y. Gong, and G. Wang, "Induced transparency in nanoscale plasmonic resonator systems," Opt. Lett. **36**, 3233–3235 (2011).
54. Z. H. Han and S. I. Bozhevolnyi, "Plasmon-induced transparency with detuned ultracompact Fabry-Perot resonators in integrated plasmonic devices," Opt. Express **19**, 3251–3257 (2011).
55. G. Wang, H. Lu, and X. Liu, "Dispersionless slow light in MIM waveguide based on a plasmonic analogue of electromagnetically induced transparency," Opt. Express **20**, 20902–20907 (2012).
56. H. Lu, X. Liu, G. Wang, and D. Mao, "Tunable high-channel-count bandpass plasmonic filters based on an analogue of electromagnetically induced transparency," Nanotechnology **23**, 444003 (2012).
57. X. S. Lin and X. G. Huang, "Tooth-shaped plasmonic waveguide filters with nanometeric sizes," Opt. Lett. **33**, 2874–2876 (2008).
58. A. Taflove and S. C. Hagness, *Computational Electrodynamics: The Finite-Difference Time-Domain Method*, 2nd ed. (Artech House, 2000).
59. Y. Cui and C. Zeng, "Optical bistability based on an analog of electromagnetically induced transparency in plasmonic waveguide-coupled resonators," Appl. Opt. **51**, 7482–7486 (2012).
60. H. Lu and X. M. Liu, "Optical bistability in subwavelength compound metallic grating," Opt. Express **21**, 13794–13799 (2013).
61. N. Liu, M. Mesch, T. Weiss, M. Hentschel, and H. Giessen, "Infrared perfect absorber and its application as plasmonic sensor," Nano Lett. **10**, 2342–2348 (2010).